UNIVERSITYOF BIRMINGHAM

Combining in-situ fluorometry and distributed rainfall data provides new insights into natural organic matter transport dynamics in an urban river

Croghan, Danny; Khamis, Kieran; Bradley, Chris; Van Loon, Anne F.; Sadler, Jon; Hannah, David M.

Document Version
Publisher's PDF, also known as Version of record

[Link to publication on Research at Birmingham portal](#)

Combining *in-situ* fluorometry and distributed rainfall data provides new insights into natural organic matter transport dynamics in an urban river

Danny Croghan [a,b,*], Kieran Khamis [a], Chris Bradley [a], Anne F. Van Loon [a,c], Jon Sadler [a], David M. Hannah [a]

[a] School of Geography, Earth and Environmental Sciences, University of Birmingham, Edgbaston, Birmingham, B15 2TT, United Kingdom of Great Britain and Northern Ireland
[b] Water Resources and Environmental Engineering, University of Oulu, Oulu, FI-90014, Finland
[c] Institute for Environmental Studies, Vrije Universiteit Amsterdam, 1081 HV Amsterdam, Netherlands

HIGHLIGHTS

- *In-situ* NOM monitoring combined with spatially distributed rainfall data
- Chemodynamic behavior for NOM only at low flows with no dominant hysteresis type
- Antecedent conditions and land-cover weighted precipitation predicted NOM.
- Potential to use land cover and high-resolution data to better understand NOM

GRAPHICAL ABSTRACT
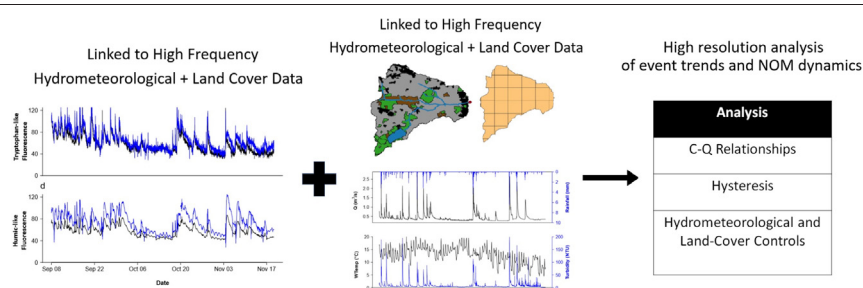
ARTICLE INFO

ABSTRACT

Urbanization alters the quality and quantity of Dissolved Organic Matter (DOM) fluxes to rivers potentially leading to water quality problems and impaired ecosystem function. Traditional synoptic and point sampling approaches are generally inadequate for monitoring DOM source dynamics. To identify links between spatial heterogeneity in precipitation and DOM dynamics, we used a unique approach combining high spatial and temporal resolution precipitation datasets featuring point, catchment, and land-cover weighted precipitation to characterise catchment transport dynamics. These datasets were linked to fluorescence records from an urban stream (Bourn Brook, Birmingham, UK). Humic-like fluorescence (HLF: Ex. 365 nm, Em. 490 nm) and Tryptophan-like fluorescence (TLF: Ex. 285 nm, Em. 340 nm) were measured, (plus river flow and turbidity) at 5 min intervals for 10 weeks during Autumn 2017. The relationship between discharge (Q) and concentration (C) for TLF and HLF were strongly chemodynamic at low Q (<Q50) but TLF was chemostatic when Q exceeded this threshold. Figure of eight hysteresis was the most common response type for both HLF and TLF, indicating that DOM sources shift within and between events. Key drivers of DOM dynamics were identified using regression analysis and model outputs using point, catchment-averaged, and land-use weighted precipitation were compared. Antecedent rainfall was identified as the most important predictor (negative relationship) of TLF and HLF change suggesting DOM source exhaustion. Precipitation weighted by land cover showed that urbanization metrics were linked to increased TLF:HLF ratios and changes in hysteresis index. This study presents a novel approach of using land-cover weighted rainfall to enhance mechanistic understanding of DOM controls and sources. In contrast, catchment-average rainfall data have the potential to yield stronger understanding of TLF dynamics. This technique could be integrated with existing high resolution *in-situ* datasets to enhance our understanding of DOM dynamics in urban rivers.

* Corresponding author at: Water Resources and Environmental Engineering, University of Oulu, Oulu, FI-90014, Finland.
E-mail address: dxc959@alumni.bham.ac.uk (D. Croghan).

1. Introduction

Dissolved Organic Matter (DOM) represents a pool of complex, heterogeneous material within the carbon cycle that is ubiquitous in riverine systems and critical for ecosystem functioning (Fellman et al., 2010; Hudson et al., 2007). DOM composition and concentration is controlled by a combination of geology, land cover, hydrometeorology and *in-situ* conditions such as biological communities and geomorphology (Coble, 1996; Williams et al., 2010). Urbanization can substantially alter catchment permeability, the drainage network, decomposition and the input of terrestrial soil/vascular plant sources of DOM, leading to a distinctive DOM composition in catchments (Hosen et al., 2014; Kaushal et al., 2014; Khamis et al., 2018). This is primarily a microbially-derived signal comprising proteinaceous compounds, whereas rural systems are typically dominated by humic-like compounds (Baker, 2001; Hosen et al., 2014; Kaushal et al., 2018; McElmurry et al., 2014; Smith and Kaushal, 2015). The increased concentration of proteinaceous compounds in urban rivers can contribute to increased biochemical oxygen demand (BOD) and oxygen depletion with negative impacts on ecosystem functioning (Kaushal et al., 2014; Khamis et al., 2017; Paerl et al., 1998). Urban DOM composition can vary at event-based time scales when changes in water-flow pathways associated with the activation of storm drains and combined sewage overflows (CSOs) can occur, connecting the wider catchment and the sewerage system to the stream (Czemiel Berndtsson, 2010; Liu et al., 2019; Zwolsman and van Bokhoven, 2007). Despite increasing urbanization worldwide (McGrane, 2016), the study of urban DOM has been relatively neglected to date. Improved understanding of the major controls on urban DOM dynamics are required to improve water quality management in urbanized catchments (Carstea et al., 2020; Khamis et al., 2020, 2018; Vaughan et al., 2019).

Both hydrometeorology (*e.g.* antecedence) and catchment land cover (particularly impervious *vs.* pervious surfaces) can influence DOM responses to individual storm events (Blaen et al., 2017; Eckard et al., 2017; Kaushal et al., 2014; McElmurry et al., 2014). For example, hydrometeorological conditions have previously been shown to be a major control on water quality dynamics (Blaen et al., 2017; Worrall and Burt, 2004). During storm events the potential nutrient load generated from the catchment is constrained by precipitation amount and intensity, while the subsequent in-stream discharge response can mobilize DOM (Saraceno et al., 2009; Schuster et al., 2007). Antecedent conditions have been highlighted as particularly important controls on nutrient dynamics. Drier conditions lead to build-up of terrestrial organic material (*e.g.* leaf litter) and the formation of biofilms in drainage infrastructure which can be mobilized during storm events, while consistently wet conditions have often been linked to source depletion, and to a subdued in-stream DOM response (Carstea et al., 2010, 2009; Khamis et al., 2020; Vaughan et al., 2019).

Land cover represents an important control on DOM response dynamics (*e.g.* total flux and composition) during storm events (McElmurry et al., 2014). The characteristics of precipitation events can be highly variable across catchments, particularly in urban catchments (Croghan et al., 2018), hence, DOM may be generated disproportionately at specific points in the catchment (Pedersen et al., 2010). Engineered headwaters, such as storm drains, gutters and pipes can act as sinks for organic material during dry periods but also provide large amounts of carbon and nitrogen to streams during storm events (Fork et al., 2018; Smith and Kaushal, 2015). Hence, in-stream responses are likely to be at least partly controlled by catchment land cover in areas where DOM is predominantly mobilized. To date, however, our ability to assess the nature of these controls on urban DOM has been constrained by the limited availability of high temporal resolution data (Blaen et al., 2016; Old et al., 2019). Furthermore, urban land use has been treated as one broad class in previous studies, while urban land cover is heterogeneous, with a range of urban metrics influencing hydrological signals (McGrane, 2016).

Fluorescence spectroscopy (excitation emission matrix; EEM) provides detailed characterization of DOM samples, and can be used to assess DOM concentration and quality (Fellman et al., 2010; Hudson et al., 2007). Continued development of optical sensor technologies, including field-deployable *in-situ* fluorometers (Carstea et al., 2020; Downing et al., 2012; Khamis et al., 2020, 2018; Saraceno et al., 2017, 2009) have enabled DOM surrogates to be monitored at high temporal resolution. Hence, DOM dynamics in flashy, urban systems can now be captured at much higher temporal resolutions (Downing et al., 2012; Saraceno et al., 2017). Previous studies in urban areas have monitored Tryptophan-like fluorescence (TLF) and Humic-like fluorescence (HLF) wavelength pairs (Khamis et al., 2020, 2018). The TLF signal is associated with dissolved proteinaceous and phenolic compounds (Beggs and Summers, 2011) but in urban rivers it is dominated by proteinaceous material (Baker, 2001). TLF is indicative of organic pollution within streams and strongly correlates with Biochemical Oxygen Demand (Baker and Inverarity, 2004). It has previously been found to be a useful water quality metric in urban streams (Khamis et al., 2017). HLF is associated with humic substances and provides a proxy for Dissolved Organic Carbon (DOC) (Coble, 1996). However, while *in-situ* fluorometers have been demonstrated to better inform DOM dynamics in urban systems, the technology has yet to be linked to spatially distributed rainfall which can provide more insight into DOM source activation across heterogeneous urban catchments.

Given the research gaps outlined above, our primary aim in this study was to identify the main controls on DOM dynamics (*i.e.* changes in composition and quantity) during high flow conditions for an urban river. To provide new mechanistic understanding of DOM transport and mobilization during storm events dynamics we used a novel approach combining *in-situ* fluorescence monitoring with high-resolution radar precipitation data. This enabled us to assess how the spatial patchiness of precipitation drives intra- (and inter-) event variability in the connectivity of different land cover units (as DOM sources are activated). By developing land-use weighted precipitation totals for storm events we aimed to highlight how this can improve our ability to predict DOM dynamics from meteorological inputs and ultimately link DOM dynamics to water routing through engineered drainage infrastructure from discrete parts of the catchment. Our objectives were to:

1) identify the main controls on DOM dynamics during storm events using high frequency, *in-situ* monitoring of humic-like fluorescence (HLF), and tryptophan-like fluorescence (TLF);

2) infer source and flow-path linkages based on DOM response to spatially resolved meteorological and land-use variables.

2. Methods

2.1. Study site

The study was conducted during in autumn 2017 from Sept. 9 to Nov. 21. Sensors were installed in the Bourn Brook, Birmingham, UK (52°27′N, 1°54′W; Fig. 1), a headwater stream with a catchment area of ~21 km^2 and elevations ranging from 116 m to 234 m above m.s.l. Although the source of the stream lies in a semi-natural woodland, the catchment is dominated by urban land cover (*i.e.* 77% urban/suburban land cover). The Bourn Brook has a flashy river flow regime, typical of urbanized catchments. There is no wastewater treatment plant in the catchment but the river receives periodic discharges from CSOs and leakage from the sewerage network (Carstea et al., 2009; Khamis et al., 2017). Chemical water quality in the river has previously been assessed by the UK Environment Agency as "good" while biological quality was "fair", although the river is at risk of diffuse pollution (Carstea et al., 2009).
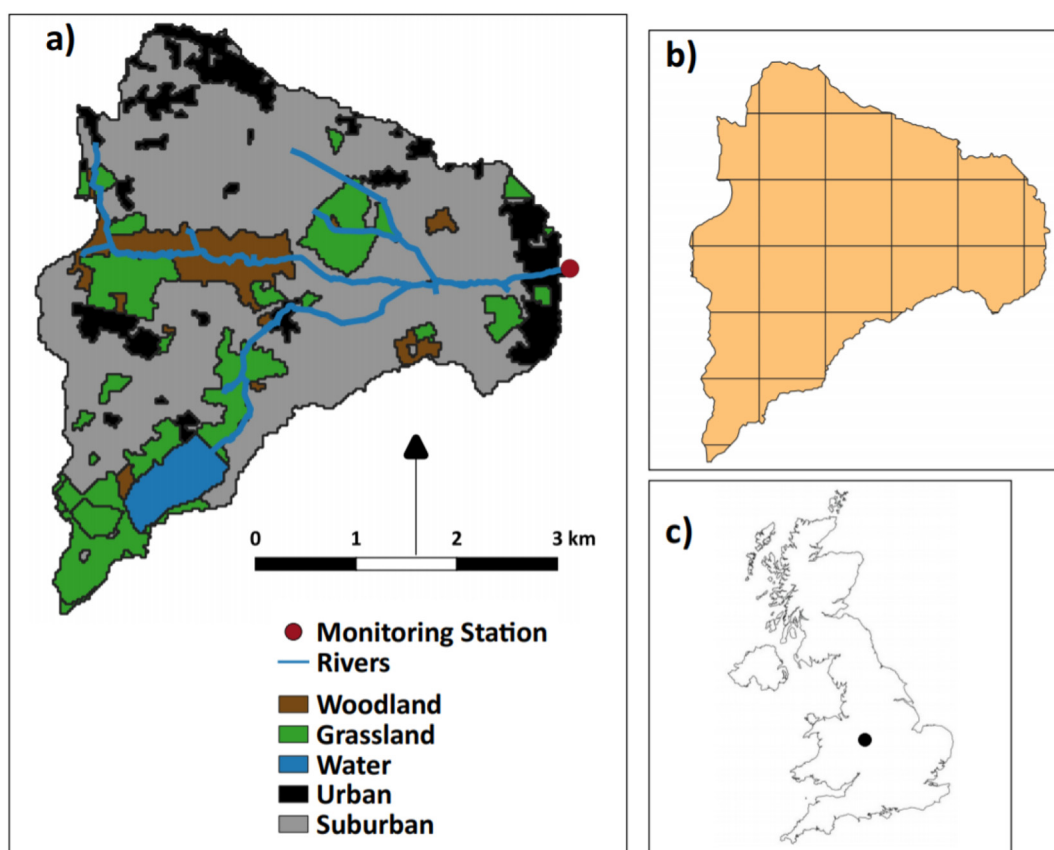
Fig. 1. A) The Bourn Brook catchment and associated land cover derived from the UK Centre of Ecology and Hydrology (CEH) Land Class 2015 (Rowland et al., 2017). B) The distribution of 1 km² grid cells used to estimate rainfall loads from rainfall radar C) The location of the catchment within the UK.

2.2. Stream data

Stream water levels were logged at 5-min resolution over the monitoring period (Sept. 9th to Nov. 21st 2017) using a Druck PDCR800 pressure transducer (GE, Billerica, USA). Water levels were converted from stage to discharge using a flow rating curve developed for the site, following the velocity-area method (n = 12). All data from the study were stored on a CR1000 data logger (Campbell Scientific, Logan, USA). A TinyTag Aquatic 2 (Gemini, Sussex, UK) water temperature logger was also installed to monitor in-stream water temperature data (Table S1 in supplementary information).

A modified GGUN-FL30 fluorometer (Albillia, Neuchâtel, Switzerland) was used to measure *in-situ* fluorescence. The sensor is composed of an excitation branch and a detection branch, which runs perpendicular to the excitation branch (Khamis et al., 2017). The instrument monitors wavelength pairs corresponding TLF, HLF, and turbidity (Table S1 in supplementary information). Turbidity was used to correct for fluorescence interference post-monitoring. Sample temperature was measured within the measurement cell using an internal thermistor enabling post-hoc correction for thermal quenching.

The fluorometer was secured on the stream bank and water samples were taken from the stream at 5-min intervals. A peristaltic pump (Model 810, Williamson Pumps Ltd., UK) controlled by a CR1000 logger was connected to the sensor and operated through a relay switch. Water samples passed through an inlet strainer wrapped in a 250-micron mesh to reduce fouling, before flowing through 3 m of silicon tubing (6.4 mm diameter) to the sensor. To minimize contamination between subsequent measurements, samples were pumped through the fluorometer for 3 min to ensure complete flushing of the measurement cell and tubing before taking three replicate measurements. Optical sensors are prone to fouling (biological and inorganic) during field deployment, particularly following storm events (Rode et al., 2016), and hence the optical

measurement cell of the sensor was cleaned at regular intervals over the monitoring period (*i.e.* sub-weekly) to reduce fouling-related drift in measurements. When fouling-related drift was identified by step changes in measurements following cleaning, the drift was corrected using a linear regression model assuming a constant fouling rate.

2.3. Instrument calibration and data correction

Raw outputs from the FL 30 (mV) were converted to ppb or NTU using a six-point calibration curve, over a range of 0–1000 ppb. Prior to each run, a blank fluorometer reading was taken using ultrapure water to assess the baseline reading. TLF was calibrated using standards created by dilution of a 100-ppm stock solution (L-Tryptophan, Acgros Organics, 99%). HLF was calibrated using quinine sulphate dehydrate in 0.05 M H_2SO_4, a 100-ppm stock solution was subsequently diluted by ultra-pure milli-Q water. Turbidity was calibrated using a formazine suspension. For all optical parameter's calibration was conducted using 1, 10, 50, 500, and 1000 ppb/NTU standard solutions, which were used immediately after production to avoid deterioration. Each solution was measured in the fluorometer for at least 1 min with measurements recorded every 10 s and a mean value taken (n ≥ 6). All measurements were taken at 20 °C, and the fluorometer was acid washed and rinsed repeatedly with deionized water between samples to avoid contamination.

Post-monitoring corrections for temperature quenching and turbidity interference were also required. Instrument-specific temperature corrections and instrument- and site-specific turbidity corrections were developed for the instrument and site prior to this study (see Khamis et al., 2017), and these were used herein. The equation for temperature quenching was derived from controlled laboratory tests following Khamis et al. (2017, 2015). River water was taken from the study site, and warmed in an incubator for 6 h over a temperature range of 5–20 °C. The *in-situ* fluorometer used in the study took

measurements of HLF and TLF at a 3-minute resolution. Ordinary least squares regression (OLS) was used to derive the correction model, with fluorescence intensity for HLF and TLF standardized to 20 °C. Fluorescence was temperature corrected to a reference temperature of 20 °C using the following equation derived by Khamis et al. (2015):

$$Fref = \frac{Fmes}{1 + p(T_{mes} - T_{ref})} \tag{1}$$

where F = Fluorescence signal, F_{mes} = measured value, p = quotient (m/c) at the reference temperature, and T_{ref} = reference value. Turbidity corrections were made for HLF and TLF using regression models developed by Khamis et al. (2017) Briefly, sediment from the study site and was used to create dilution calibration series ranging from 0 to 500 NTU and the percentage change in the HLF and TLF signal across the range of turbidities used to correct the fluorescence signal.

To validate the fluorometer data, samples were regularly taken from the river during the study period by a pump sampler for analysis in the laboratory. Samples were filtered through 0.45 μm sterile nylon membranes and analyzed within 24 h. A Cary Eclipse Spectrofluorometer was used to analyze samples for fluorescence. A raman blank was measured prior to analysis, and an ultrapure blank was also taken. Excitation-Emission Matrices (EEMs) were then produced for each sample. Data was then corrected for blank, raman normalization, and inner-filter effects using the "*eemR*" package. Sample peaks corresponding to the TLF and HLF wavelengths used in this study were then extracted. Comparison of the values from the lab analyzed samples compared to the *in-situ* fluorometer showed a good relationship (Fig. S1 in supplementary material) for both TLF ($R^2 = 0.64$) and HLF ($R^2 = 0.68$). Precision of the fluorescence measurements was assessed by triplicate measurement of 30 subsamples. For both TLF and HLF, precision (one standard deviation) was ±4%.

2.4. Meteorological data

Two sources of precipitation data were used in the study: station-derived precipitation data (hereafter referred to as point precipitation data), which provides rainfall totals for a single point in the study catchment, and radar rainfall data which allows catchment-average precipitation to be calculated for each event. Point precipitation data were recorded at hourly time steps using an Automatic Weather Station located ~1 km from the study site (see Khamis et al., 2020). Radar precipitation data were recorded at 5-min time steps at 1 km² spatial resolution enabling spatial estimates of precipitation to be produced for each storm for 1 km² grid cells distributed across the catchment (Fig. 1B) (Croghan et al., 2018). Estimates of precipitation totals falling on each land cover type were then derived (refer to Section 2.5.2) for further data analysis. We also calculated precipitation amounts for each storm event calculated up to the point of maximum HLF and TLF, as overall event rainfall totals are an inaccurate estimate of the amount of rainfall that has occurred at the point of maximum TLF and HLF.

2.5. Data analysis

2.5.1. Concentration-discharge data

C-Q relationships were developed for HLF and TLF. The C-Q relationship was determined by calculating the slope on logarithmically transformed data for both C and Q, as has been widely used in prior concentration-discharge studies (Bieroza et al., 2018; Evans and Davies, 1998; Godsey et al., 2009). HLF, TLF, and discharge were log-transformed and regressed against flow to determine slope. Where the slope is <0.1, the relationship is defined as chemostatic, meaning that no change in concentrations occurs with increasing discharge. Conversely, for slopes >0.1, the relationship is chemodynamic, indicating either a dilution or concentration effect with increasing discharge (Bieroza et al., 2018).

As the C-Q relationships we observed were not linear, we also used segmented regression to test for breakpoints in the C-Q relationships (Muggeo, 2008). These were validated using the Davies test and by comparing the fit of the linear and segmented model (Akaike Information Criterion; AIC).

Hysteresis analysis provides further information about the nature of the C-Q relationship during discrete storm events, specifically the potential catchment source areas and flow pathways (Lloyd et al., 2016a; Vaughan et al., 2017). In this case we used the modified Hysteresis Index (HI) developed by Lloyd et al. (2016b). The modified HI calculates hysteresis across the loop for different flow percentiles by comparing the rising limb and falling limb values. Due to the rapid rising limb flow, which is common in urban rivers (Fletcher et al., 2013), the percentiles ranged from 20% to 33%. In calculating the modified HI, discharge (Q) and fluorescence (F) for both HLF and TLF were normalized using the following equation (Lloyd et al., 2016a, 2016b), taking Q as an example:

$$Normalised\ Q_i = \frac{Q_i - Q_{min}}{Q_{max} - Q_{min}} \tag{2}$$

where Q_i is discharge for a given timestep, Q_{min} is minimum discharge and Q_{max} is maximum discharge. Fluorescence values were normalized in the same manner and HI was calculated using the following equation:

$$HI_i = V_r - V_f \tag{3}$$

where HI_i is the HI for a given percentile, V_r is the value of the rising limb for a given variable, and V_f is the corresponding value of the falling limb for the given variable. All values across the loop were then averaged, yielding an HI value between −1 and 1 for each event. Positive (negative) values indicate clockwise (anti-clockwise) hysteresis.

Each event hysteresis graph was visually inspected and classified, based on directionality and shape, into one of the following groups: (i) figure of eight, (ii) clockwise, (iii) anti-clockwise, (iv) complex, and (v) no hysteresis, which previous studies have suggested are the most common forms of hysteresis (Williams, 1989).

2.5.2. Hydrometeorological and landscape analysis

Events were defined using the "*hydromad*" R package, using a threshold of >25% increase in flow for a minimum of 5 h. This relatively short event duration was selected given the flashy nature of the catchment. Hydrometeorological and landscape metrics (Table 1) were determined for 22 events.

Hydrometeorological metrics were chosen *a priori* based on their importance in previous water quality studies (Blaen et al., 2017). Land cover variables that reflected the drainage properties of the basin and influence water flow pathways were selected (Khamis et al., 2018), including: percentage road cover (defined as road and associated paved surfaces), roofs (defined as roof area from all buildings in the catchment), urban area (defined as all paved surfaces within the catchment), vegetation (defined as all vegetation within the catchment including woodland), and woodland (defined as only wooded areas of the catchment). Vegetation, woodland, and urbanization metrics were calculated at 25 m² spatial resolution using the Centre of Ecology and Hydrology Land Class 2015 dataset (Rowland et al., 2017), while road and roof cover data were obtained from the Urban Atlas 2012 dataset at a minimum spatial resolution of 10 m² (EEA, 2012).

To identify the impact of catchment land cover on DOM storm dynamics, we undertook a novel approach linking high spatial and temporal resolution precipitation data to high spatial resolution land cover data. The intention was to investigate landscape links to DOM dynamics and determine whether this can inform better understanding of pathways and sources of DOM. To do this, the catchment was sub-divided into 1 km² grid cells corresponding to the radar precipitation dataset grid cells (Fig. 1B). For each event, precipitation totals were determined for

Table 1
Summary of hydrometeorological and landscape metrics analyzed. Land cover stats represent the contribution of each land cover type during individual events. Descriptive statistics are shown for storm events within the study period.

Variable	Code	Metric	Unit	Max	Min	Mean ± SD
Flow	PF	Peak flow	m³ s⁻¹	2.79	0.54	1.46 ± 0.77
	ED	Event duration	Hours	58.00	5.75	23.55 ± 14.15
Point precipitation	PRA	Rainfall amount	mm	18.40	0.40	5.57 ± 4.95
	PMax	Maximum hourly intensity	mm/h	6.40	0.40	2.11 ± 1.64
	PMean	Mean intensity	mm/h	2.57	0.18	0.72 ± 0.51
Catchment precipitation	CRA	Rainfall amount	mm	3.46	0.8	3.45 ± 3.21
	CMax	Maximum hourly intensity	mm/h	4.66	0.12	1.23 ± 0.96
	CMean	Mean intensity	mm/h	3.82	0.08	0.87 ± 0.93
Temperature	WT	Water temperature during event	°C	14.50	9.33	12.37 ± 1.34
Antecedent conditions	1A	Total rain 1 day before event	mm	5.60	0	1.31 ± 1.72
	7A	Total rain 7 days before event	mm	31.20	2.20	18.84 ± 9.27
	14A	Total rain 14 days before event	mm	46.40	4.80	32.68 ± 12.47
	EM	Magnitude of last event	m³ s⁻¹	2.79	0.54	1.43 ± 0.79
Landscape	Ur	Average urbanized	%	78.16	73.36	75.79 ± 1.14
	Ve	Average vegetation	%	28.09	20.94	24.95 ± 1.75
	Wo	Average woodland	%	9.86	5.87	6.96 ± 0.77
	Ro	Average roofs	%	11.44	10.84	11.16 ± 0.16
	Rd	Average roads	%	8.36	8.00	8.21 ± 0.11

each grid cell, and the weighted average for the contribution of each grid cell to the total event rainfall was derived. The contributions of each land cover type in every event were calculated as a function of the proportional land cover in each grid cell and each grid cell was weighted by the proportion of the total catchment precipitation that fell in that grid cell (hereafter termed land-cover weighted precipitation). Grid cell values were then averaged to yield a single value for each land cover variable representing its estimated contribution to each event and indicating the relative precipitation totals falling on roads, vegetation, urban areas, roofed, and woodland areas during each event.

To assess the relationship between the hydrometeorological and landscape predictors (Table 1) and the fluorescence metrics (Table S2 in supplementary information), ordinary least squares (OLS) multiple linear regression was undertaken. Three different starting models

were chosen: a point-precipitation, catchment-average precipitation model, and land-cover weighted precipitation model. The difference in the models lay in the use of the precipitation metric which sought to investigate the strength of associations between fluorescence metrics and point precipitation, catchment averaged precipitation, and precipitation linked to the land cover datasets. For the fluorescence metrics relating to maximum TLF and HLF, precipitation data were calculated to the point maximum TLF and HLF occurred, while for the other fluorescence metrics, precipitation data were calculated as event totals. Variables were initially screened for normality and homogeneity of variance using Shapiro-Wilk tests (Shapiro and Wilk, 1965), and then visually inspected using quantile-quantile plots. All variables were found to be normally distributed. Data were then investigated for collinearity by calculating variance influence factors (VIF) (Zuur et al., 2010). If a
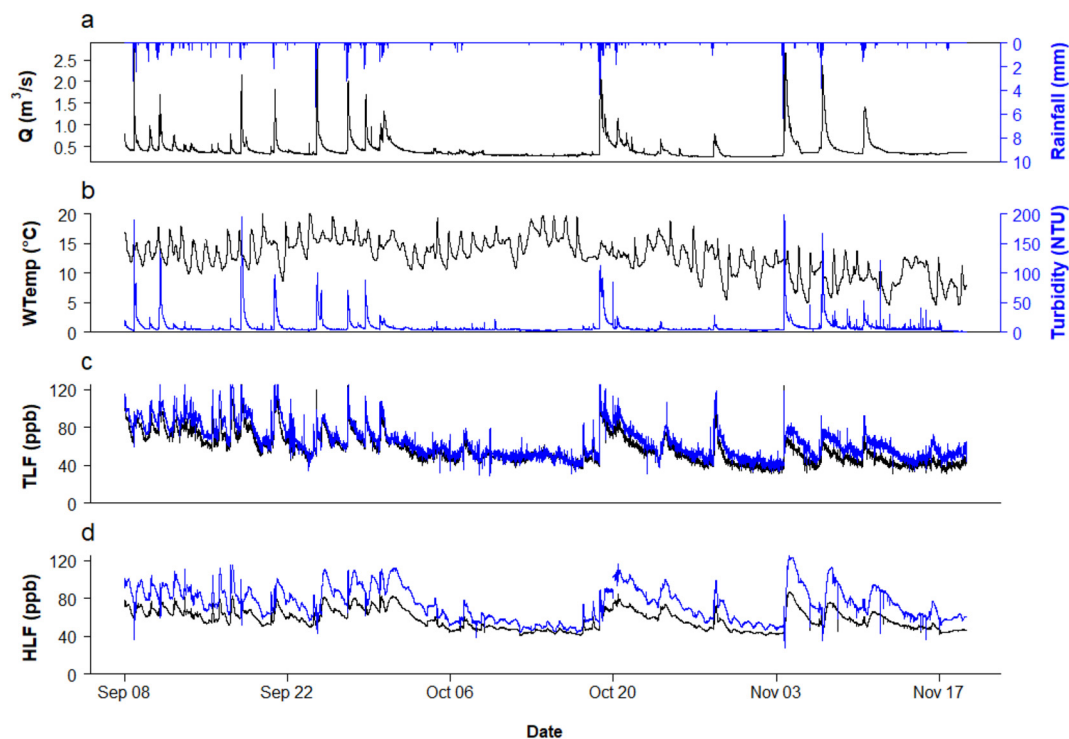
Fig. 2. Time series of water quality and stream discharge for the study period: 9 Sept. to 21 Nov. 2017: A) gives discharge (black) and precipitation (blue); B) presents water temperature (black) and turbidity (blue); C) shows tryptophan-like fluorescence (TLF); and D) shows humic-like fluorescence (HLF). For TLF and HLF black lines show the data corrected for temperature quenching and turbidity interference, and blue lines show the raw time series.

variable had a VIF >3, it was removed from the analysis. The R package "MuMIn" was then used to fit all combinations of response models (N = 256) ranked according to corrected AICc due to the small sample size of the dataset. All models with <2AICc were considered the subset of best models. Where no clear best model was apparent, model averaging was used to calculate standardized regression coefficients as weighted averages. To compare which model set had the highest explanatory capability, the R^2 was calculated for the model with the highest weight (see Supplementary material) for each metric.

3. Results

3.1. Water quality parameter time series

During the study period daily mean discharge was 0.43 ± 0.17 m^3 s^{-1} and 22 discrete storm events were identified. Baseflow was relatively stable for the duration of the study, with discharge peaks associated with individual precipitation events (Fig. 2). Mean precipitation for each discrete event averaged 5.57 ± 4.95 mm, with the bulk of studied events (14) occurring in September, followed by a drier period from the 1st to the 20th October, followed by a further 5 events in quick succession. In November, 3 discrete precipitation events were identified (Fig. 2). Water temperature (WTemp) showed a notable decrease over time during the study (Fig. 2): from a mean daily WTemp of 14.21 ± 2.13 °C in September to 9.5 ± 2.33 °C in November.

Turbidity remained low during baseflow, with peaks during storm events (Fig. 2). TLF was also stable outside of storm events, with increases that largely corresponded with the onset of the event (Fig. 2). Mean daily TLF was 61 ± 15.85 ppb, with a maximum daily mean of 85.9 ppb recorded on 11 September. Uncorrected TLF was slightly higher than corrected TLF, with uncorrected mean daily TLF at 64.47 ± 17.3 ppb. HLF was also stable during baseflow, although a slight diurnal pattern was evident with decreases in HLF during the day and increases at night (Fig. 2). Mean daily HLF was 58.05 ± 10.65 ppb, with a maximum daily mean of 76.39 ppb observed on 1 October. Uncorrected daily HLF was higher than corrected HLF, with uncorrected mean daily HLF at 74.35 ± 17.67 ppb.

3.2. Concentration controls

3.2.1. Concentration-discharge analysis

Analysis of the C-Q relationship indicates that both TLF ($P < 0.01$, slope $= 0.54 \pm 0.01$) and HLF ($P < 0.01$, slope $= 0.30 \pm 0.01$) exhibited significant chemodynamic behavior (Fig. 3). The relationship was stronger for TLF, with greater explanatory power for the TLF linear model ($R^2 = 0.40$) compared to the HLF linear model ($R^2 = 0.36$), For both TLF and HLF a segmented regression model (TLF $R^2 = 0.52$ and HLF $R^2 = 0.68$) had greater explanatory power than the linear model (TLF $R^2 = 0.40$, HLF $R^2 = 0.36$). For TLF data (Fig. 3a), a break point was identified at 0.48 ± 0.01 m^3 s^{-1} (Davies test $P < 0.001$, $\Delta_{AIC} = 4628$) with chemodynamic behavior observed below (slope $= 0.85 \pm 0.01$) and chemostatic behavior above (slope $= 0.09 \pm 0.01$) this point. For HLF, a break point was apparent at 0.46 ± 0.01 m^3 s^{-1} (Davies test $P < 0.001$, $\Delta_{AIC} = 14{,}412$) with a corresponding shift from chemodynamic to chemostatic behavior observed.

3.2.2. Hysteresis analysis

Four forms of hysteresis were observed during the study period (Fig. 4). An HI between -0.1 and 0.1 was most commonly observed for both the HLF (11 events) and TLF (8 events) datasets (Table 2). An HI of <-0.1 (indicating anti-clockwise hysteresis) was found for 8 events for TLF, and for 9 events for HLF. An event HI of >0.1 (clockwise hysteresis) was found 6 times for the TLF dataset, but only two times for the HLF dataset.

After visual inspection, figure of eight hysteresis was determined to be the most common class in both datasets, followed by anti-clockwise,
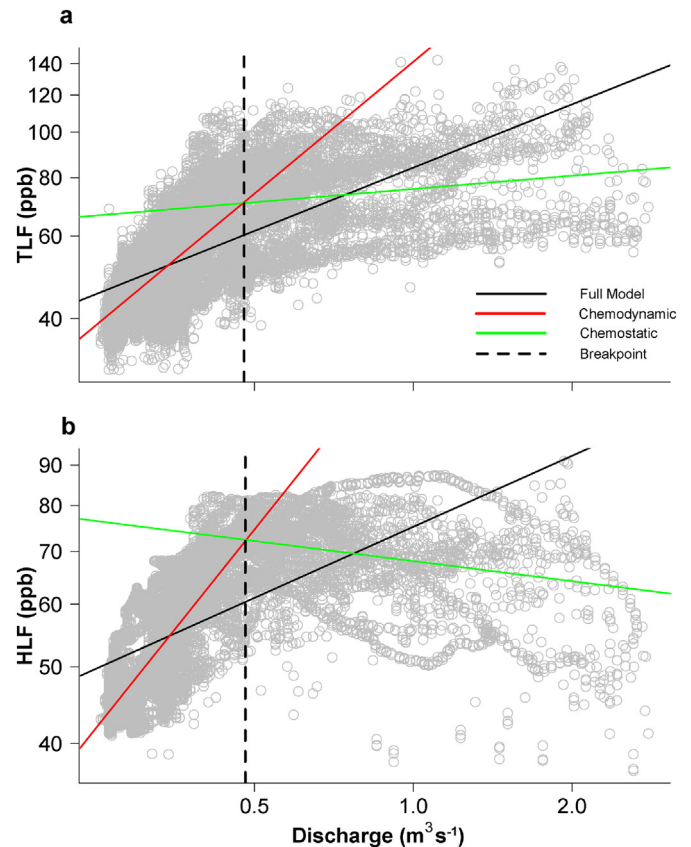
Fig. 3. Log C-Q relationship for a) tryptophan-like fluorescence (TLF) against discharge and b) humic-like fluorescence (HLF) against discharge (right). Overall C-Q relationships for the dataset are indicated by the black lines, red lines show the chemodynamic portion of the dataset, and green lines show the chemostatic. The breakpoint line (±0.01 m^3 s^{-1}) indicates where the relationship changes from chemodynamic to chemostatic.

with clockwise hysteresis occurring far less frequently for both datasets (Table 2). While the HI suggested clockwise hysteresis events were most frequent, most clockwise and anti-clockwise hysteresis events were reclassified as figure of eight hysteresis following visual inspection. Complex hysteresis was also common in both datasets and tended to occur during storm events with multiple discharge peaks on the rising limb of the event.

3.3. Landscape and hydrometeorological controls

3.3.1. Point-source model

Antecedent condition variables were the dominant predictor of maximum fluorescence for the point precipitation models (Table 3). All models aside from mean TLF:HLF ratio, and HLF HI were found to be significant. Strong negative associations were found with seven-day antecedent precipitation (effect size ranging from -0.33 to -0.65). One-day antecedent rainfall was a less strong predictor compared to seven-day antecedent rainfall and only correlated with HLF metrics, with weaker effect sizes found. Water temperature was also found to be strongly associated with maximum TLF (0.45) and maximum HLF (0.50). Point precipitation metrics were moderately associated with maximum fluorescence metrics (0.32–0.45). Explanatory power was higher for the TLF models compared to the HLF models (R^2 increase of 0.14 in the maximum TLF model compared to the HLF model, and an increase of 0.09 in the maximum TLF percentage change model compared to the corresponding HLF model).

In contrast, the mean TLF:HLF ratio was most strongly associated with the point precipitation metric (Table 3; −0.37), while positive associations were found for one day antecedent rainfall (0.28) and water temperature (0.24), however the explanatory power of this model was very weak ($R^2 = 0.09$).

For the hysteresis metrics there was no correlation with antecedence (Table 3). TLF HI was positively associated with peak flow (0.45) and precipitation (0.49), however no other hydrometeorological predictors featured in the best models for HLF HI. While the TLF HI model showed weak to moderate explanatory capability ($R^2 = 0.20$), no result was determined for the HLF HI model because no predictors featured in the model.

3.3.2. Catchment average precipitation model

In the catchment average precipitation model (Table 4), the associations between the TLF metrics and precipitation were stronger than for the point-precipitation model (Table 4). All models aside from the HLF HI model were found to be significant predictors of fluorescent metrics. Catchment average precipitation featured as a predictor for Max TLF with a moderate positive association (0.24). For other metrics featuring TLF, catchment average precipitation model consistently increased effect size compared to the point-precipitation model. Catchment precipitation therefore appeared to be a strong predictor of the percentage increase in maximum TLF (increase of 0.09 compared to the point model), mean TLF:HLF ratio (increase of 0.40) and TLF HI (increase of
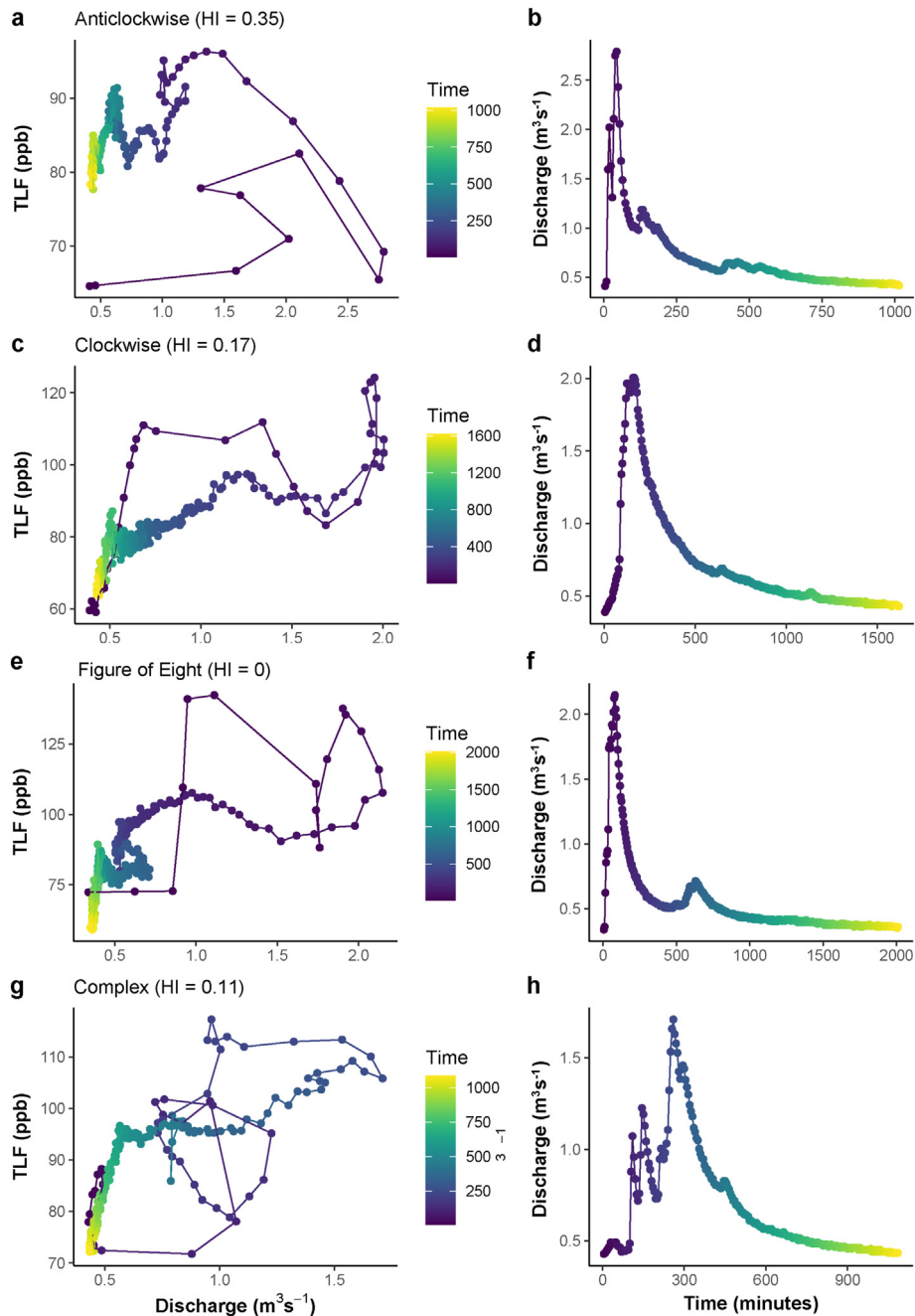

Fig. 4. Examples of the hysteresis types observed during the study period (a,c,e,g), with the associated event-hydrograph shown to the right of each hysteresis type (b,d,f,h). Colour of the data points relates to the progression of the event (yellow = event start, red = event end). The associated HI scores are shown for each graph.

Table 2
HI shows categories for individual events for both TLF and HLF. The hysteresis categories were split as follows: >0.1 (indicating clockwise hysteresis), −0.1-0.1 (indicating no hysteresis), and <−0.1 (indicating anti-clockwise hysteresis). Hysteresis type shows the categorization of events into the four defined hysteresis categories. Hysteresis type was determined by visual inspection as a means of best identifying figure of eight hysteresis.

	HI			Hysteresis type			
	>0.1	0.1 to −0.1	<−0.1	Clockwise	Anti-clockwise	Figure of eight	Complex
TLF	6	8	8	2	7	8	5
HLF	2	11	9	0	8	9	5

0.08). Furthermore, explanatory capability was improved in the maximum TLF percentage model (increase in R^2 of 0.07), and in the mean TLF:HLF ratio model (increase in R^2 of 0.15), while for the TLF HI model only a modest increase was observed (increase in R^2 of 0.03).

In contrast, for the HLF metrics relationships with catchment average precipitation were less strong. The catchment average precipitation did not appear as a predictor in the Max HLF model, while for the maximum HLF percentage change the association was reduced compared to the point precipitation model. However, as the main predictors of HLF metrics were antecedent conditions, the predictive power of the top model for Max HLF showed no difference, while the Max HLF percentage change showed minimal difference compared to the point model (decrease in R^2 of 0.03).

3.3.3. Precipitation by land cover weighted precipitation model

When incorporating land cover weighted precipitation, all models were significant. However, for the maximum fluorescence metrics land cover weighted precipitation did not feature in the best models, which were dominated by antecedent conditions predictors (Table 5). The explanatory capability of the land cover weighted precipitation models was similar to the point and catchment models for the maxi-

mum fluorescence metrics (no change in R^2 for the TLF max, and a reduction of 0.04 for the HLF max models). Furthermore, Residual standard error (RSE) was higher in the HLF max land cover weighted model compared to the point and catchment precipitation models (Tables 3–5). For the maximum percentage change models however, the land cover weighted precipitation models showed substantially less predictive capability (lower R^2 by 0.12 compared to the catchment model for the TLF maximum percentage change, and lower by 0.11 compared to the HLF maximum percentage change models). In comparison to the other model sets (Tables 3–5), RSE was highest for both the and HLF land cover weighted precipitation models.

For the mean TLF:HLF model, urbanization (0.44) and road density (0.37) were positively associated with mean TLF:HLF. Urbanization extent was found to have the strongest association with mean TLF:HLF of all model variables in the complex model, although this association was not as strong as catchment average precipitation in the catchment average precipitation model (Table 5). Land cover predictors also appeared in both HI models, with road density (−0.35) weakly negatively associated with TLF HI, however urbanization was found to be positively associated with TLF HI (0.42). The only model to find a predictor for HLF HI was the land-use model, with road density positively associated (0.51) with HLF HI, while urbanization was negatively associated with HLF HI (−0.44). A significant higher explanatory capability was found by using land cover weighted precipitation for the mean TLF:HLF ratio compared to the point data set (increase of R^2 of 0.05), although this was less than the catchment dataset. RSE was lower for the land cover weighted TLF:HLF model compared to the point model, but higher than the catchment model (Tables 3–5). The highest explanatory capability for HI in the dataset was found by the land cover weighted precipitation data, with a slight increase compared to the catchment TLF HI model (R^2 increase of 0.01), while as the only parameter set to produce a final model, a minor explanatory value was found for the HLF HI (R^2 = 0.12). RSE was also found to be lower for the TLF HI model in the land cover weighted models compared to the point and catchment models (Tables 3–5).

Table 3
Results of model selection for the point-precipitation dataset. Standardized regression model effect sizes are shown for each variable in each model. R^2 and RSE (Residual Standard Error) are shown for the top model for each metric. Standard error (±) is also shown. The predictor codes refer to the following: 7A = seven-day antecedent rainfall, 1A = one-day antecedent rainfall, WT = water temperature during event, PF = peak flow, PRA = point rainfall amount. * = P < 0.05, ** = P < 0.01, *** = P < 0.001. All models <2 ΔAICc of the top model are presented in Table S3 in supplementary material.

Response	Point predictors					R^2	RSE
	7A	1A	WT	PF	PRA		
Max TLF	−0.57 ± 0.16		0.45 ± 0.16			0.48***	0.72
Max HLF	−0.33 ± 0.18	−0.36 ± 0.19	0.50 ± 0.19		0.32 ± 0.20	0.34**	0.81
Max TLF increase (%)	−0.65 ± 0.12				0.36 ± 0.12	0.76***	0.49
Max HLF increase (%)	−0.51 ± 0.16	−0.22 ± 0.20		−0.27 ± 0.15	0.45 ± 0.16	0.67***	0.57
Mean TLF:HLF ratio		0.28 ± 0.21	0.24 ± 0.22	−0.25 ± 0.22	−0.37 ± 0.20	0.09	0.95
TLF HI				0.46 ± 0.20	0.49 ± 0.19	0.20*	0.89
HLF HI						NA	NA

Table 4
Results of model selection for the catchment-average precipitation dataset. Standardized regression model effect sizes are shown for each variable in each model. R^2 and RSE (Residual Standard Error) are shown for the top model for each metric. Standard error (±) is also shown. The predictor codes refer to the following: 7A = seven-day antecedent rainfall, 1A = one-day antecedent rainfall, WT = water temperature during event, PF = peak flow, CRA = catchment rainfall amount, CMax = catchment maximum rainfall intensity. * = P < 0.05, ** = P < 0.01, *** = P < 0.001. All models <2 ΔAICc of the top model are presented in Table S4 in supplementary material.

Response	Catchment predictors						R^2	RSE
	7A	1A	WT	PF	CRA	CMax		
Max TLF	−0.53 ± 0.17		0.42 ± 0.16		0.24 ± 0.17	0.23 ± 0.18	0.48***	0.72
Max HLF	−0.39 ± 0.18	−0.36 ± 0.18	0.50 ± 0.18				0.34**	0.81
Max TLF increase (%)	−0.58 ± 0.11				0.49 ± 0.14	−0.16 ± 0.14	0.83***	0.41
Max HLF increase (%)	−0.51 ± 0.18	−0.22 ± 0.15			0.34 ± 0.15		0.63***	0.61
Mean TLF:HLF ratio	−0.32 ± 0.22				−0.77 ± 0.35	0.43 ± 0.27	0.24*	0.87
TLF HI				0.46 ± 0.20	0.58 ± 0.26	−0.32 ± 0.30	0.23*	0.88
HLF HI							NA	NA

Table 5

Results of model selection for the precipitation by land-use dataset. Standardized regression model effect sizes are shown for each variable in each model. R^2 and RSE (Residual Standard Error) are shown for the top model for each metric. Standard error ($\pm$) is also shown. The predictor codes refer to the following: 7A = seven-day antecedent rainfall, 1A = one-day antecedent rainfall, WT = water temperature during event, PF = peak flow, Rd = road density, Urb = Urbanization extent. * = P < 0.05, ** = P < 0.01, *** = P < 0.001. All models <2 ΔAICc of the top model are presented in Table S5 in supplementary material.

Response	Land cover weighted predictors						R^2	RSE
	7A	1A	WT	PF	Rd	Urb		
Max TLF	−0.58 ± 0.16		0.45 ± 0.16				0.48***	0.72
Max HLF	−0.33 ± 0.20		0.50 ± 0.19	−0.23 ± 0.12			0.30*	0.84
Max TLF increase (%)	−0.72 ± 0.16	−0.20 ± 0.13		0.27 ± 0.14			0.71***	0.56
Max HLF increase (%)	−0.73 ± 0.16			0.19 ± 0.15			0.56***	0.66
Mean TLF:HLF ratio		0.30 ± 0.20	0.30 ± 0.20		0.37 ± 0.20	0.44 ± 0.20	0.14*	0.93
TLF HI	−0.41 ± 0.20	−0.30 ± 0.19		0.43 ± 0.20	0.35 ± 0.23	−0.44 ± 0.23	0.24*	0.87
HLF HI				−0.32 ± 0.20	0.51 ± 0.20	−0.44 ± 0.21	0.12	0.94

4. Discussion

The results highlight that the headwater urban systems exhibit a low breakpoint in the C-Q relationship, showing the potential for hysteresis effects to be a strong control on DOM dynamics in the urban headwaters. By using a novel approach incorporating high spatial and temporal resolution precipitation datasets, we have shown that choice of precipitation dataset may yield stronger relationships in the hydrometeorological controls on DOM dynamics. By incorporating land use weighted precipitation into the dataset, it has been possible to highlight links between land cover weighted precipitation and hysteresis. Using this dataset in combination with the catchment precipitation data yielded stronger relationships than the traditional approach of using point precipitation data.

4.1. Controls on DOM concentration

We found that TLF and HLF responses were chemodynamic when discharge was below a certain threshold, suggesting that in our catchment, small events may have a disproportionately large impact on DOM dynamics. Urban catchments have particularly strong terrestrial-riverine linkages with drainage systems becoming active at relatively low precipitation totals, although urban catchments are also largely disconnected from subsurface pathways which limits microbial processing (McGrane, 2016). Consequently, even small events (<1 mm) can have substantial TLF and HLF fluxes (Kaushal and Belt, 2012). The strong changes in TLF and HLF at low discharge suggest that significant sources of organic fluorophores, contributing to both TLF and HLF, are either instream or situated close to the channel. Previous studies have indicated that storm drain biofilms are particularly rich sources of DOM, while road runoff may also be associated with an elevated DOM pulses (Zhao et al., 2015). Stream bed scouring has also been proposed as an important DOM source during storm events with benthic algae and biofilms transported (Kaushal and Belt, 2012; Khamis et al., 2018). The chemostatic nature of the relationship at higher discharge is likely a result of a variety of factors. To a certain extent, it will reflect a dilution effect, whereby increased runoff from flow pathways carrying DOM are counteracted by low DOM precipitation inputs, leading to a relatively steady chemostatic relationship. As a result, the high HLF and TLF concentrations at low discharge are likely to be a result of anti-clockwise hysteresis, as observed by Evans and Davies (1998). It should also be noted that the range of values observed at high discharge is very high, indicating that events of similar magnitude have a substantially different response in DOM concentration. This suggests that antecedent conditions may be a major control of DOM dynamics for higher discharge events (Guarch-Ribot and Butturini, 2016; Yates et al., 2016). While when antecedent conditions are wetter, new flow paths may develop over the wider catchment, thereby creating new DOM sources of DOM within the drainage network (Haga et al., 2005), in this study it was demonstrated that DOM was suppressed at higher antecedent rainfall

suggesting wet antecedent conditions contributed to a exhaustion effect from the main contributing sources in the catchment (Khamis et al., 2020).

The hysteresis analysis identified a range of hysteresis types in the catchment. Figure of eight hysteresis was most commonly observed for both TLF and HLF. As discharge increases from initially low values, clockwise hysteresis occurs, possibly as in- or near-stream DOM sources are activated, while at higher discharges, anti-clockwise hysteresis occurs as a result of the changing relationship between discharge and DOM (Lloyd et al., 2016a, 2016b). This is possibly due to source depletion from the near-stream sources that are activated first during storm flow (Lawler et al., 2006). It also appears that the fluorophores contributing to TLF are more prone to source depletion, whereas those for HLF remain elevated even after the return to baseflow suggesting a long-term input from distal sources (Vaughan et al., 2017). This may reflect the contribution of slow subsurface, waterflow pathways which provide a steady and constant input of humic material. In contrast, the organic compounds contributing to TLF appear to be more related to proximal sources, reflecting the influence of engineered structures on TLF. The latter accumulate protein-like materials over time (Sakrabani et al., 2009), but are susceptible to exhaustion effects which can cause clockwise hysteresis. While anti-clockwise hysteresis occurred regularly in both HLF and TLF, this suggests a lag between rising discharge and DOM activation, which suggests that distal pathways are a prominent DOM source. The presence of anti-clockwise hysteresis may also result from the activation and cross-connections of CSOs, which are inactive at the beginning of the event and are activated only during heavy rainfall when specific flow thresholds are exceeded (Chen et al., 2017).

Furthermore, TLF can be quenched by humic like compounds as a result of intermolecular energy transfer between these compounds (Wang et al., 2015). The effects of humic compounds quenching proteinaceous materials can be substantial. Wang et al. (2015) identified quenching of protein like compounds by humic materials of 35–52% when NOM concentration in a mixture was approximately 10 mg/L. Resultantly, the TLF signal observed during this study may represent an underestimate of the actual TLF signal in this study catchment, particularly during storm events when NOM concentrations increase. Due to the potential importance of inputs from sources with high concentrations of proteinaceous compounds such as CSOs, it is important to note that the impacts and prevalence of these are likely to be substantially dulled by the prevalence of humic-like material in the system. Resultantly, the importance of TLF-sources in this already TLF dominated system is likely to be even greater than shown within this study.

4.2. Hydrometeorological and landscape controls on DOM dynamics

Our results highlight that antecedent rainfall is the strongest predictor of the maximum increase in fluorescence. Antecedent rainfall conditions featured in all maximum fluorescence models, following numerous studies showing that antecedent conditions act to control

nutrient dynamics (Blaen et al., 2017; Gnecco et al., 2005; Grand-Clement et al., 2014). This provides further evidence that source depletion is linked to antecedent conditions. Wetter antecedent periods lead to source depletion, with regular rainfall events leading to DOM exhaustion (Carstea et al., 2009). During drier conditions organic material builds up in the catchment, which can be subsequently mobilized during events (Guarch-Ribot and Butturini, 2016).

Water temperatures were also found to be a dominant control of maximum TLF and HLF suggesting that temperature has an important role in DOM delivery and uptake (Huang et al., 2013; Raymond et al., 2016; Winterdahl et al., 2016, 2011). Higher temperatures drive increased biological activity and increased algal production within streams which is a key DOM source (Dawson et al., 2008). TLF and HLF were higher at the start of the study (early Autumn) and lower values at the end of the study (late Autumn) and the water temperature changes observed may also reflect seasonal changes. Hence, the reductions in HLF and TLF that we observed in later events could be related to seasonal changes such as changes in leaf fall within early Autumn (Miller and McKnight, 2010).

The TLF: HLF ratio was strongly negatively associated with precipitation metrics. This suggests that the urban river is more dominated by TLF (compared to HLF) during smaller events, while HLF predominates during larger events. This is likely because the main sources of organic compounds contributing to TLF are associated with the storm drainage system, hence an efficient storm drainage network can deliver comparatively large influxes of TLF even during low precipitation events (Baker, 2001; Carstea et al., 2009; Mendoza et al., 2020). Further, HLF tends to remain elevated longer than TLF the longer a storm event lasts likely due to the influence of sub-surface sources which tend to be dominated by humic-like materials (Khamis et al., 2018). Precipitation was also strongly positively associated to the TLF HI, which indicates that at higher precipitation, clockwise hysteresis was more prevalent. This provides additional evidence that the compounds contributing to TLF are more vulnerable to source depletion, while no association was found between precipitation and HLF HI.

While hydrometeorological conditions appear to represent the dominant control on changes in maximum DOM dynamics, the inclusion of land cover weighted precipitation improved model fits for hysteresis and ratios which provides greater insights into some of the more nuanced aspects of DOM dynamics and may improve accuracy for source zone tracking. By using land cover weighted precipitation data, a better understanding of the relative contribution of different land use types to the OM flux could be gained. As urban land use has been previously linked to strong hysteresis effects and has previously been demonstrated to be more vulnerable to exhaustion effects (Khamis et al., 2020; Lawler et al., 2006; Vaughan et al., 2017), by weighting precipitation to land use metrics, greater understanding of the direct links between urbanized sources links to hysteresis metrics was observed in this study.

In the mean TLF:HLF model, the extent of urbanization was found to be the main control indicating that urbanization leads to increasing TLF predominance in the river. This supports previous work on the TLF:HLF ratio which suggested that the TLF:HLF ratio could be used to identify the anthropogenic impact on streams (Baker and Inverarity, 2004). Where stormwater discharge is generated predominantly on urbanized surfaces, it is likely to activate numerous sources contributing to TLF, and subsequently enter the engineered storm drainage network (Carstea et al., 2010; Fork et al., 2018), hence contributing to the system becoming increasingly dominated by compounds contributing to urbanization and road density and TLF HI, which suggests that lower HI is observed more at higher urbanization. This likely reflects that there are more sources of compounds relating to TLF where urbanization is higher which increase the opportunity for clockwise hysteresis (Carstea et al., 2020; Vaughan et al., 2019, 2017), while at lower urbanization there is increasing clockwise hysteresis due to finite material for transport (*i.e.* greater potential source depletion). Interestingly, the only

model which found a predictor for HLF HI was the land cover model where HLF HI was positively associated with road density. This suggests that at higher road densities, higher HI values occur which may be because where storm drains are an increasing source of DOM into the stream (Khamis et al., 2020), the compounds contributing to HLF are more likely to be from anthropogenic sources which are particularly prone to source depletion when compared to natural sub-surface flow paths (Vaughan et al., 2019, 2017). However, while the results here suggest there are promising links between land cover weighted precipitation, however, further work is needed across a broader range of catchments. Due to the distance of non-urban land cover from the measurement point in the study catchment, it is likely that the associated landscape signal found was weakened due the longer travel time of and increased potential for mixing and in-stream processing to occur when compared to runoff close to the measurement point. Resultantly, as most the non-urban land cover in the catchment was in the outer boundaries of the catchment, the importance of the land cover signal may have been reduced. Hence, it is possible that the impact of non-urban land cover on DOM dynamics was underestimated in this study. Furthermore, dynamic landscapes (forests or agricultural land) has previously been shown to be a prominent cause of seasonal shifts in DOM composition (Shatilla and Carey, 2019). However, due to the relatively short-term timescale of this study it is unlikely we observed seasonal shifts in DOM associated with changes in landscape processes (*e.g.* from bud-burst *vs* leaf fall). Hence, to yield stronger relationships with land cover, longer term studies across multiple seasons are required.

No association between land cover weighted precipitation metrics was found for the maximum amount of fluorescence observed which suggests that hydrometeorological factors, particularly antecedent conditions, influence the quantity of organic material available for export (Carstea et al., 2020; Khamis et al., 2020). The strongest associations between maximum TLF related metrics were with the catchment-average rainfall data which suggests the importance of incorporating high spatial and temporal resolution precipitation data to better understand TLF related dynamics in urban streams. This is likely because the TLF response appears to be more directly linked to rainfall dynamics as TLF tends to be dominated by surface, or shallow sub-surface sources (Khamis et al., 2018), therefore capturing accurate catchment average precipitation yields stronger associations by more accurately reflecting catchment wide precipitation run-off. In contrast, maximum HLF metrics were dominated by antecedent conditions hence explanatory value remained the same between the point and catchment precipitation datasets.

5. Conclusions

This study applied a novel approach using high-resolution rainfall radar datasets to highlight the main controls on DOM event dynamics and explored the links to organic matter sources and transport mechanisms. To our knowledge, this is the first use of high-resolution rainfall data for this purpose and offers a unique insight into the impact of precipitation and landscape data on DOM dynamics for a small urban headwater system.

We found that the urban river behaves chemodynamically at lower discharge, but at higher discharge source depletion and dilution lead to the system becoming chemostatic. The relatively low discharge required for large increases in DOM suggested terrestrial DOM inputs to the stream represent regular, recurrent events regardless of event size, however it should also be considered that the time of year may also have influenced the results of the study. Further, we highlight the importance of antecedent conditions in controlling urban DOM dynamics, particularly in relation to the maximum quantity of DOM entering the system. This suggests that source depletion is a predominant driving mechanism of urban DOM dynamics. Precipitation also provided a moderate control on DOM, although this influence varied depending upon how precipitation was estimated. TLF-related metrics appear strongly

related to high spatial and temporal resolution precipitation datasets, while HLF metrics were more strongly related to point precipitation data which highlights the need to incorporate both estimates in future work. We also showed that hydrometeorological controls were generally the main control of increases in fluorescence, however land cover weighted helped unravel more nuanced changes in DOM behavior by providing stronger information about the nature of hysteresis relationships. The potential for land cover weighted precipitation data to help constrain our understanding of OM source zone activation in highly heterogeneous catchments is clear.

CRediT authorship contribution statement

Danny Croghan: Conceptualization, Writing - original draft, Methodology, Visualization, Formal analysis, Data curation, Project administration, Resources, Investigation, Writing - review & editing. **Kieran Khamis:** Conceptualization, Writing - review & editing, Methodology, Visualization, Data curation, Project administration, Investigation, Resources, Supervision. **Chris Bradley:** Conceptualization, Writing - review & editing, Resources, Supervision. **Anne F. Van Loon:** Supervision, Writing - review & editing. **Jon Sadler:** Supervision, Writing - review & editing. **David M. Hannah:** Supervision, Conceptualization, Resources, Funding acquisition.

Declaration of competing interest

The authors declare that they have no known competing financial interests or personal relationships that could have appeared to influence the work reported in this paper.

Acknowledgements

Appendix A. Supplementary data

Supplementary data to this article can be found online at https://doi.org/10.1016/j.scitotenv.2020.142731.

References

Baker, A., 2001. Fluorescence excitation-emission matrix characterization of some sewage-impacted rivers. Environ. Sci. Technol. 35, 948–953.

Baker, A., Inverarity, R., 2004. Protein-like fluorescence intensity as a possible tool for determining river water quality. Hydrol. Process. 18, 2927–2945. https://doi.org/10.1002/hyp.5597.

Beggs, K.M.H., Summers, R.S., 2011. Character and chlorine reactivity of dissolved organic matter from a mountain pine beetle impacted watershed. Environ. Sci. Technol. 45, 5717–5724. https://doi.org/10.1021/es1042436.

Bieroza, M.Z., Heathwaite, A.L., Bechmann, M., Kyllmar, K., Jordan, P., 2018. The concentration-discharge slope as a tool for water quality management. Sci. Total Environ. 630, 738–749. https://doi.org/10.1016/J.SCITOTENV.2018.02.256.

Blaen, P.J., Khamis, K., Lloyd, C.E.M., Bradley, C., Hannah, D., Krause, S., 2016. Real-time monitoring of nutrients and dissolved organic matter in rivers: capturing event dynamics, technological opportunities and future directions. Sci. Total Environ. 569–570, 647–660. https://doi.org/10.1016/J.SCITOTENV.2016.06.116.

Blaen, P.J., Khamis, K., Lloyd, C., Comer-Warner, S., Ciocca, F., Thomas, R.M., MacKenzie, A.R., Krause, S., 2017. High-frequency monitoring of catchment nutrient exports reveals highly variable storm event responses and dynamic source zone activation. J. Geophys. Res. Biogeosci. 122, 2265–2281. https://doi.org/10.1002/2017JG003904.

Carstea, E.M., Baker, A., Pavelescu, G., Boomer, I., 2009. Continuous fluorescence assessment of organic matter variability on the Bournbrook River, Birmingham, UK. Hydrol. Process. 23, 1937–1946. https://doi.org/10.1002/hyp.7335.

Carstea, E.M., Baker, A., Bieroza, M., Reynolds, D., 2010. Continuous fluorescence excitation–emission matrix monitoring of river organic matter. Water Res. 44, 5356–5366. https://doi.org/10.1016/j.watres.2010.06.036.

Carstea, E.M., Popa, C.L., Baker, A., Bridgeman, J., 2020. In situ fluorescence measurements of dissolved organic matter: a review. Sci. Total Environ. https://doi.org/10.1016/j.scitotenv.2019.134361.

Chen, H., Liao, Z., Gu, X., Xie, J., Li, H., Zhang, J., 2017. Anthropogenic influences of paved runoff and sanitary sewage on the dissolved organic matter quality of wet weather overflows: an excitation–emission matrix parallel factor analysis assessment. Environ. Sci. Technol. 51, 1157–1167. https://doi.org/10.1021/acs.est.6b03727.

Coble, P.G., 1996. Characterization of marine and terrestrial DOM in seawater using excitation-emission matrix spectroscopy. Mar. Chem. 51, 325–346. https://doi.org/10.1016/0304-4203(95)00062-3.

Croghan, D., Van Loon, A.F., Sadler, J.P., Bradley, C., Hannah, D.M., 2018. Prediction of river temperature surges is dependent on precipitation method. Hydrol. Process. https://doi.org/10.1002/hyp.13317.

Czemiel Berndtsson, J., 2010. Green roof performance towards management of runoff water quantity and quality: a review. Ecol. Eng. 36, 351–360. https://doi.org/10.1016/J.ECOLENG.2009.12.014.

Dawson, J.J.C., Soulsby, C., Tetzlaff, D., Hrachowitz, M., Dunn, S.M., Malcolm, I.A., 2008. Influence of hydrology and seasonality on DOC exports from three contrasting upland catchments. Biogeochemistry 90, 93–113. https://doi.org/10.1007/s10533-008-9234-3.

Downing, B.D., Pellerin, B.A., Bergamaschi, B.A., Saraceno, J.F., Kraus, T.E.C., 2012. Seeing the light: the effects of particles, dissolved materials, and temperature on in situ measurements of DOM fluorescence in rivers and streams. Limnol. Oceanogr. Methods 10, 767–775. https://doi.org/10.4319/lom.2012.10.767.

Eckard, R.S., Pellerin, B.A., Bergamaschi, B.A., Bachand, P.A.M., Bachand, S.M., Spencer, R.G.M., Hernes, P.J., 2017. Dissolved organic matter compositional change and biolability during two storm runoff events in a small agricultural watershed. J. Geophys. Res. Biogeosci. 122, 2634–2650. https://doi.org/10.1002/2017JG003935.

EEA, 2012. Corine Land Cover 2012.

Evans, C., Davies, T.D., 1998. Causes of concentration/discharge hysteresis and its potential as a tool for analysis of episode hydrochemistry. Water Resour. Res. 34, 129–137. https://doi.org/10.1029/97WR01881.

Fellman, J.B., Hood, E., Spencer, R.G.M., 2010. Fluorescence spectroscopy opens new windows into dissolved organic matter dynamics in freshwater ecosystems: a review. Limnol. Oceanogr. 55, 2452–2462. https://doi.org/10.4319/lo.2010.55.6.2452.

Fletcher, T.D., Andrieu, H., Hamel, P., 2013. Understanding, management and modelling of urban hydrology and its consequences for receiving waters: a state of the art. Adv. Water Resour. 51, 261–279. https://doi.org/10.1016/j.advwatres.2012.09.001.

Fork, M.L., Blaszczak, J.R., Delesantro, J.M., Heffernan, J.B., 2018. Engineered headwaters can act as sources of dissolved organic matter and nitrogen to urban stream networks. Limnol. Oceanogr. Lett. 3, 215–224. https://doi.org/10.1002/lol2.10066.

Gnecco, I., Berretta, C., Lanza, L.G., La Barbera, P., 2005. Storm water pollution in the urban environment of Genoa, Italy. Atmos. Res. 77, 60–73. https://doi.org/10.1016/J.ATMOSRES.2004.10.017.

Godsey, S.E., Kirchner, J.W., Clow, D.W., 2009. Concentration-discharge relationships reflect chemostatic characteristics of US catchments. Hydrol. Process. 23, 1844–1864. https://doi.org/10.1002/hyp.7315.

Grand-Clement, E., Luscombe, D.J., Anderson, K., Gatis, N., Benaud, P., Brazier, R.E., 2014. Antecedent conditions control carbon loss and downstream water quality from shallow, damaged peatlands. Sci. Total Environ. 493, 961–973. https://doi.org/10.1016/J.SCITOTENV.2014.06.091.

Guarch-Ribot, A., Butturini, A., 2016. Hydrological conditions regulate dissolved organic matter quality in an intermittent headwater stream. From drought to storm analysis. Sci. Total Environ. 571, 1358–1369. https://doi.org/10.1016/J.SCITOTENV.2016.07.060.

Haga, H., Matsumoto, Y., Matsutani, J., Fujita, M., Nishida, K., Sakamoto, Y., 2005. Flow paths, rainfall properties, and antecedent soil moisture controlling lags to peak discharge in a granitic unchanneled catchment. Water Resour. Res. 41. https://doi.org/10.1029/2005WR004236.

Hosen, J.D., McDonough, O.T., Febria, C.M., Palmer, M.A., 2014. Dissolved organic matter quality and bioavailability changes across an urbanization gradient in headwater streams. Environ. Sci. Technol. 48, 7817–7824. https://doi.org/10.1021/es501422z.

Huang, W., McDowell, W.H., Zou, X., Ruan, H., Wang, J., Li, L., 2013. Dissolved organic carbon in headwater streams and riparian soil organic carbon along an altitudinal gradient in the Wuyi Mountains, China. PLoS One 8, e78973. https://doi.org/10.1371/journal.pone.0078973.

Hudson, N., Baker, A., Reynolds, D., 2007. Fluorescence analysis of dissolved organic matter in natural, waste and polluted waters—a review. River Res. Appl. 23, 631–649. https://doi.org/10.1002/rra.1005.

Kaushal, S.S., Belt, K.T., 2012. The urban watershed continuum: evolving spatial and temporal dimensions. Urban Ecosyst. 15, 409–435. https://doi.org/10.1007/s11252-012-0226-7.

Kaushal, S.S., McDowell, W.H., Wollheim, W.M., 2014. Tracking evolution of urban biogeochemical cycles: past, present, and future. Biogeochemistry 121, 1–21. https://doi.org/10.1007/s10533-014-0014-y.

Kaushal, S.S., Gold, A.J., Bernal, S., Johnson, T.A.N., Addy, K., Burgin, A., Burns, D.A., Coble, A.A., Hood, E., Lu, Y., Mayer, P., Minor, E.C., Schroth, A.W., Vidon, P., Wilson, H., Xenopoulos, M.A., Doody, T., Galella, J.G., Goodling, P., Haviland, K., Haq, S., Wessel, B., Wood, K.L., Jaworski, N., Belt, K.T., 2018. Watershed 'chemical cocktails': forming novel elemental combinations in Anthropocene fresh waters. Biogeochemistry 141, 281–305. https://doi.org/10.1007/s10533-018-0502-6.

Khamis, K., Sorensen, J.P.R., Bradley, C., Hannah, D.M., Lapworth, D.J., Stevens, R., 2015. In situ tryptophan-like fluorometers: assessing turbidity and temperature effects for freshwater applications. Environ Sci Process Impacts 17, 740–752. https://doi.org/10.1039/C5EM00030K.

Khamis, K., Bradley, C., Stevens, R., Hannah, D.M., 2017. Continuous field estimation of dissolved organic carbon concentration and biochemical oxygen demand using dual-wavelength fluorescence, turbidity and temperature. Hydrol. Process. 31, 540–555. https://doi.org/10.1002/hyp.11040.

Khamis, K., Bradley, C., Hannah, D.M., 2018. Understanding dissolved organic matter dynamics in urban catchments: insights from *in situ* fluorescence sensor technology. Wiley Interdiscip. Rev. Water 5, e1259. https://doi.org/10.1002/wat2.1259.

Khamis, K., Bradley, C., Hannah, D.M., 2020. High frequency fluorescence monitoring reveals new insights into organic matter dynamics of an urban river, Birmingham, UK. Sci. Total Environ. 710. https://doi.org/10.1016/j.scitotenv.2019.135668.

Lawler, D.M., Petts, G.E., Foster, I.D.L., Harper, S., 2006. Turbidity dynamics during spring storm events in an urban headwater river system: the upper tame, west midlands, UK. Sci. Total Environ. 360, 109–126. https://doi.org/10.1016/j.scitotenv.2005.08.032.

Liu, C., Du, Y., Yin, H., Fan, C., Chen, K., Zhong, J., Gu, X., 2019. Exchanges of nitrogen and phosphorus across the sediment-water interface influenced by the external suspended particulate matter and the residual matter after dredging. Environ. Pollut. 246, 207–216. https://doi.org/10.1016/j.envpol.2018.11.092.

Lloyd, C.E.M., Freer, J.E., Johnes, P.J., Collins, A.L., 2016a. Using hysteresis analysis of high-resolution water quality monitoring data, including uncertainty, to infer controls on nutrient and sediment transfer in catchments. Sci. Total Environ. 543, 388–404. https://doi.org/10.1016/J.SCITOTENV.2015.11.028.

Lloyd, C.E.M., Freer, J.E., Johnes, P.J., Collins, A.L., 2016b. Technical note: testing an improved index for analysing storm discharge-concentration hysteresis. Hydrol. Earth Syst. Sci. 20, 625–632. https://doi.org/10.5194/hess-20-625-2016.

McElmurry, S.P., Long, D.T., Voice, T.C., 2014. Stormwater dissolved organic matter: influence of land cover and environmental factors. Environ. Sci. Technol. 48, 45–53. https://doi.org/10.1021/es402664t.

McGrane, S.J., 2016. Impacts of urbanisation on hydrological and water quality dynamics, and urban water management: a review. Hydrol. Sci. J. 61, 2295–2311. https://doi.org/10.1080/02626667.2015.1128084.

Mendoza, L.M., Mladenov, N., Kinoshita, A.M., Pinongcos, F., Verbyla, M.E., Gersberg, R., 2020. Fluorescence-based monitoring of anthropogenic pollutant inputs to an urban stream in Southern California, USA. Sci. Total Environ. 718, 137206. https://doi.org/10.1016/j.scitotenv.2020.137206.

Miller, M.P., McKnight, D.M., 2010. Comparison of seasonal changes in fluorescent dissolved organic matter among aquatic lake and stream sites in the Green Lakes Valley. J. Geophys. Res. 115. https://doi.org/10.1029/2009JG000985 G00F08.

Muggeo, V.M., 2008. segmented: an R package to fit regression models with broken-line relationships. R News 8, 20–25.

Old, G.H., Naden, P.S., Harman, M., Bowes, M.J., Roberts, C., Scarlett, P.M., Nicholls, D.J.E., Armstrong, L.K., Wickham, H.D., Read, D.S., 2019. Using dissolved organic matter fluorescence to identify the provenance of nutrients in a lowland catchment; the River Thames, England. Sci. Total Environ. 653, 1240–1252. https://doi.org/10.1016/J.SCITOTENV.2018.10.421.

Paerl, H., Pinckney, J., Fear, J., Peierls, B., 1998. Ecosystem responses to internal and watershed organic matter loading: consequences for hypoxia in the eutrophying Neuse River Estuary, North Carolina, USA. Mar. Ecol. Prog. Ser. 166, 17–25.

Pedersen, L., Jensen, N.E., Christensen, L.E., Madsen, H., 2010. Quantification of the spatial variability of rainfall based on a dense network of rain gauges. Atmos. Res. 95, 441–454. https://doi.org/10.1016/j.atmosres.2009.11.007.

Raymond, P.A., Saiers, J.E., Sobczak, W.V., 2016. Hydrological and biogeochemical controls on watershed dissolved organic matter transport: pulse- shunt concept. Ecology 97, 5–16. https://doi.org/10.1890/14-1684.1.

Rode, M., Wade, A.J., Cohen, M.J., Hensley, R.T., Bowes, M.J., Kirchner, J.W., Arhonditsis, G.B., Jordan, P., Kronvang, B., Halliday, S.J., Skeffington, R.A., Rozemeijer, J.C., Aubert, A.H., Rinke, K., Jomaa, S., 2016. Sensors in the stream: the high-frequency wave of the present. Environ. Sci. Technol. 50, 10297–10307. https://doi.org/10.1021/acs.est.6b02155.

Rowland, C.S., Morton, R.D., Carrasco, L., McShane, G., O'Neil, A.W., Wood, C., 2017. Land cover map 2015. NERC Environ. Inf. Data Cent. 44, 1–25. https://doi.org/10.5285/505d1e0c-ab60-4a60-b448-68c5bbae403e.

Sakrabani, R., Vollertsen, J., Ashley, R.M., Hvitved-Jacobsen, T., 2009. Biodegradability of organic matter associated with sewer sediments during first flush. Sci. Total Environ. 407, 2989–2995. https://doi.org/10.1016/J.SCITOTENV.2009.01.008.

Saraceno, J.F., Pellerin, B.A., Downing, B.D., Boss, E., Bachand, P.A.M., Bergamaschi, B.A., 2009. High-frequency in situ optical measurements during a storm event: Assessing relationships between dissolved organic matter, sediment concentrations, and hydrologic processes. J. Geophys. Res. Biogeosciences 114. https://doi.org/10.1029/2009JG000989 G00F09.

Saraceno, J.F., Shanley, J.B., Downing, B.D., Pellerin, B.A., 2017. Clearing the waters: evaluating the need for site-specific field fluorescence corrections based on turbidity measurements. Limnol. Oceanogr. Methods 15, 408–416. https://doi.org/10.1002/lom3.10175.

Schuster, P.F., Shanley, J.B., Marvin-Dipasquale, M., Reddy, M.M., Aiken, G.R., Roth, D.A., Taylor, H.E., Krabbenhoft, D.P., DeWild, J.F., 2007. Mercury and organic carbon dynamics during runoff episodes from a Northeastern USA Watershed. Water Air Soil Pollut. 187, 89–108. https://doi.org/10.1007/s11270-007-9500-3.

Shapiro, S.S., Wilk, M.B., 1965. An analysis of variance test for normality (complete samples). Biometrika. 52, 591–611. https://doi.org/10.1093/biomet/52.3-4.591.

Shatilla, N.J., Carey, S.K., 2019. Assessing inter-annual and seasonal patterns of DOC and DOM quality across a complex alpine watershed underlain by discontinuous permafrost in Yukon, Canada. Hydrol. Earth Syst. Sci. 23, 3571–3591. https://doi.org/10.5194/hess-23-3571-2019.

Smith, R.M., Kaushal, S.S., 2015. Carbon cycle of an urban watershed: exports, sources, and metabolism. Biogeochemistry 126, 173–195. https://doi.org/10.1007/s10533-015-0151-y.

Vaughan, M.C.H., Bowden, W.B., Shanley, J.B., Vermilyea, A., Sleeper, R., Gold, A.J., Pradhanang, S.M., Inamdar, S.P., Levia, D.F., Andres, A.S., Birgand, F., Schroth, A.W., 2017. High-frequency dissolved organic carbon and nitrate measurements reveal differences in storm hysteresis and loading in relation to land cover and seasonality. Water Resour. Res. 53, 5345–5363. https://doi.org/10.1002/2017WR020491.

Vaughan, M.C.H., Bowden, W.B., Shanley, J.B., Vermilyea, A., Schroth, A.W., 2019. Shining light on the storm: in-stream optics reveal hysteresis of dissolved organic matter character. Biogeochemistry 143, 275–291. https://doi.org/10.1007/s10533-019-00561-w.

Wang, Z., Cao, J., Meng, F., 2015. Interactions between protein-like and humic-like components in dissolved organic matter revealed by fluorescence quenching. Water Res. 68, 404–413. https://doi.org/10.1016/j.watres.2014.10.024.

Williams, G.P., 1989. Sediment concentration versus water discharge during single hydrologic events in rivers. J. Hydrol. 111, 89–106. https://doi.org/10.1016/0022-1694(89)90254-0.

Williams, C.J., Yamashita, Y., Wilson, H.F., Jaffé, R., Xenopoulos, M.A., 2010. Unraveling the role of land use and microbial activity in shaping dissolved organic matter characteristics in stream ecosystems. Limnol. Oceanogr. 55, 1159–1171. https://doi.org/10.4319/lo.2010.55.3.1159.

Winterdahl, M., Futter, M., Köhler, S., Laudon, H., Seibert, J., Bishop, K., 2011. Riparian soil temperature modification of the relationship between flow and dissolved organic carbon concentration in a boreal stream. Water Resour. Res., 47 https://doi.org/10.1029/2010WR010235.

Winterdahl, M., Laudon, H., Lyon, S.W., Pers, C., Bishop, K., 2016. Sensitivity of stream dissolved organic carbon to temperature and discharge: implications of future climates. J. Geophys. Res. Biogeosci. 121, 126–144. https://doi.org/10.1002/2015JG002922.

Worrall, F., Burt, T., 2004. Time series analysis of long-term river dissolved organic carbon records. Hydrol. Process. 18, 893–911. https://doi.org/10.1002/hyp.1321.

Yates, C.A., Johnes, P.J., Spencer, R.G.M., 2016. Assessing the drivers of dissolved organic matter export from two contrasting lowland catchments, U.K. Sci. Total Environ. 569–570, 1330–1340. https://doi.org/10.1016/J.SCITOTENV.2016.06.211.

Zhao, C., Wang, C.-C., Li, J.-Q., Wang, C.-Y., Wang, P., Pei, Z.-J., 2015. Dissolved organic matter in urban stormwater runoff at three typical regions in Beijing: chemical composition, structural characterization and source identification. RSC Adv. 5, 73490–73500. https://doi.org/10.1039/C5RA14993B.

Zuur, A.F., Ieno, E.N., Elphick, C.S., 2010. A protocol for data exploration to avoid common statistical problems. Methods Ecol. Evol. 1, 3–14. https://doi.org/10.1111/j.2041-210X.2009.00001.x.

Zwolsman, J.J.G., van Bokhoven, A.J., 2007. Impact of summer droughts on water quality of the Rhine River - a preview of climate change? Water Sci. Technol. 56, 45–55. https://doi.org/10.2166/wst.2007.535.